Neuron
Article

Cellular Resolution Maps of X Chromosome Inactivation: Implications for Neural Development, Function, and Disease

Hao Wu,[1,7] Junjie Luo,[2] Huimin Yu,[1] Amir Rattner,[1] Alisa Mo,[3] Yanshu Wang,[1,7] Philip M. Smallwood,[1,7] Bracha Erlanger,[4] Sarah J. Wheelan,[4,6] and Jeremy Nathans[1,3,5,7,*]
[1]Department of Molecular Biology and Genetics
[2]Department of Biological Chemistry
[3]Department of Neuroscience
[4]Department of Oncology
[5]Department of Ophthalmology
[6]Division of Biostatistics and Bioinformatics
[7]Howard Hughes Medical Institute
Johns Hopkins University School of Medicine, Baltimore, MD 21205, USA
*Correspondence: jnathans@jhmi.edu
http://dx.doi.org/10.1016/j.neuron.2013.10.051

SUMMARY

Female eutherian mammals use X chromosome inactivation (XCI) to epigenetically regulate gene expression from ~4% of the genome. To quantitatively map the topography of XCI for defined cell types at single cell resolution, we have generated female mice that carry X-linked, Cre-activated, and nuclear-localized fluorescent reporters—GFP on one X chromosome and tdTomato on the other. Using these reporters in combination with different Cre drivers, we have defined the topographies of XCI mosaicism for multiple CNS cell types and of retinal vascular dysfunction in a model of Norrie disease. Depending on cell type, fluctuations in the XCI mosaic are observed over a wide range of spatial scales, from neighboring cells to left versus right sides of the body. These data imply a major role for XCI in generating female-specific, genetically directed, stochastic diversity in eutherian mammals on spatial scales that would be predicted to affect CNS function within and between individuals.

INTRODUCTION

For animals such as dipteran insects, birds, and mammals, in which males and females possess distinct complements of sex chromosomes, a mechanism is needed to normalize the relative levels of gene expression from the autosomes, present at two copies per somatic cell, and the shared sex chromosome, present at either one or two copies. In female mammals, this normalization is achieved by epigenetic silencing of most of the genes on one of the two X chromosomes, a process referred to as X chromosome inactivation (XCI). The discovery of XCI followed from the observation that female eutherian mammals show somatic mosaicism for traits such as coat color and that the nuclei of female somatic cells possess a condensed chromatin structure, the Barr body (Lyon, 1962).

XCI is initiated early in embryogenesis and is complete by approximately embryonic day (E) 6.5 in the mouse (with some variation among tissues; Tan et al., 1993; Sugimoto et al., 2000; Hadjantonakis et al., 2001). For XCI in embryonic tissues, the choice between maternal and paternal X chromosomes appears to be random, but in extraembryonic tissues the paternal X chromosome is selectively inactivated (Takagi and Sasaki, 1975; West et al., 1977). Since its discovery, XCI has served as a paradigm for epigenetic regulation (Lee, 2011). The intrachromosomal spreading of inactivation is controlled by a large noncoding RNA, Xist, which is transcribed from and associates in *cis* with the inactive X chromosome. The inactive chromosome is characterized by increased DNA methylation and repressive histone modifications.

In the context of human genetic disease, the implications of XCI for heterozygous females have long been recognized (reviewed in Willard, 2001). In the context of neurologic disease, the effects of XCI vary with disease (Dobyns et al., 2004). For example, carriers of hypoxanthine phosphoribosyl transferase (*HPRT*) deficiency (Lesch-Nyhan syndrome) are usually unaffected (Jinnah and Friedmann, 2001). By contrast, carriers of *MECP2* deficiency (Rett syndrome) invariably exhibit serious neurologic symptoms (Chahrour and Zoghbi, 2007).

XCI also has the potential to create cellular diversity that is advantageous. Among New World primates, polymorphic variation within a single X-linked visual pigment gene confers trichromatic color vision on females heterozygous for alleles that encode pigments with different spectral sensitivities, whereas homozygous females and hemizygous males have dichromatic color vision (Jacobs, 1998). Similarly, female mice genetically engineered to carry a pair of X-linked visual pigment alleles coding for spectrally distinct pigments acquire an added dimension of chromatic discrimination (Jacobs et al., 2007).

These observations emphasize the importance of knowing the spatial- and cell-type-specific patterns of XCI, most especially in

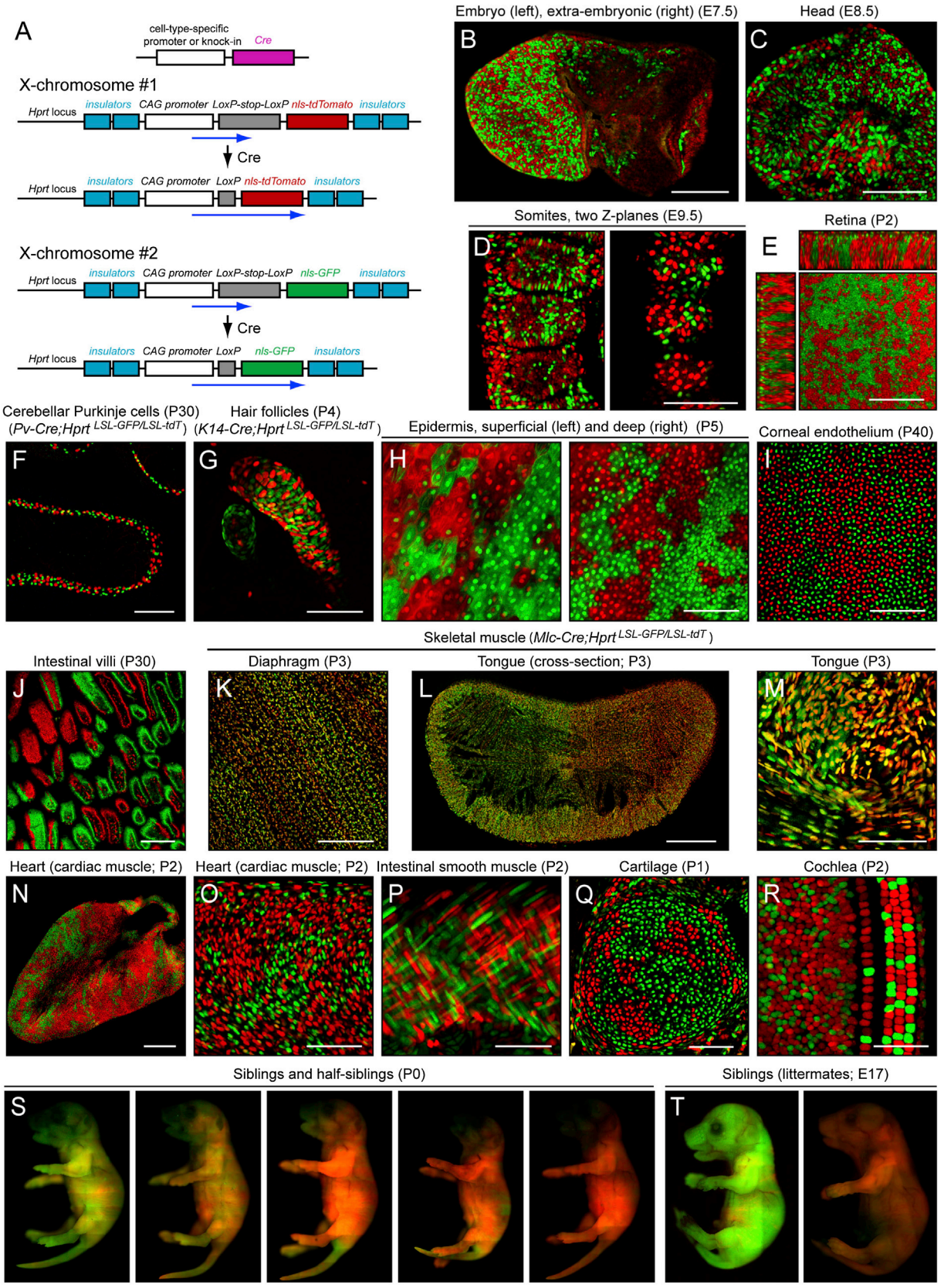

(legend on next page)

the nervous system where cell location, type, and function are tightly controlled. They also emphasize the importance of knowing which genes obey, escape, or are quantitatively influenced by XCI. The present study addresses these questions with the use of mice that have been genetically engineered to visualize XCI in defined cell types at single-cell resolution.

RESULTS

Dual Color Mouse Lines for Visualizing XCI Mosaicism at Cellular Resolution

Previous work with gene-targeted mice has shown that reporters inserted at the X-linked *Hprt* locus obey XCI (Ciavatta et al., 2006). To construct a dual color system for visualizing XCI, we modified an *Hprt* targeting vector in which tandem insulators flank a central reporter cassette, and we detected the desired gene targeting event by the restoration of Hprt activity in embryonic stem cells that carry a partial deletion of the *Hprt* gene (Ciavatta et al., 2006; Yang et al., 2009). As shown in Figure 1A, the XCI reporters consist of a *CMV/beta-actin* enhancer/promoter, a *LoxP-transcription stop-LoxP* (*LSL*) cassette, and coding sequences for a nuclear-localized fluorescent protein, either GFP or tdTomato ($Hprt^{LSL\text{-}GFP}$ and $Hprt^{LSL\text{-}tdT}$). Combining the two reporters in a heterozygous female together with a cell-type-specific *Cre* transgene or knockin allele marks the pattern of XCI in the cell type of interest. We note that this Cre-activated dual color XCI system only works in somatic tissues if the *Cre* transgene or knockin allele is not expressed in the germline, because each parent of the female test mouse must contribute one of the two *Hprt* reporters. As summarized in Table S1, this requirement was met by most but not all of the 25 cell-type-specific *Cre* lines tested. Excision of the *LSL* cassette with a germline Cre recombinase generates the constitutively active alleles $Hprt^{GFP}$ and $Hprt^{tdT}$.

A survey of various embryonic, neonatal, and adult tissues from $Hprt^{GFP/tdT}$ females provides an overview of the topography of XCI mosaicism (Figures 1B–1R; except where indicated otherwise, the images in Figure 1 are of $Hprt^{GFP/tdT}$ females). The paternal X chromosome is mostly inactivated in extraembryonic tissue (Figure 1B), as is well established (Takagi and Sasaki, 1975; West et al., 1977), and at E7.5 and E8.5 embryonic cells show finely mixed XCI mosaics (Figures 1B and 1C). At E9.5, there is clear somite-to-somite heterogeneity in the relative abundances of GFP+ (green, G) and tdT+ (red, R) cells, characterized hereafter as the [R/(R + G)] ratio (Figure 1D). The postnatal day (P)2 retina shows radially oriented zones of a single color spanning the full thickness of the retina, in keeping with previous studies of XCI and lineage tracing in the retina (Figure 1E; Fekete et al., 1994; Reese et al., 1999). Using *Pv-Cre* and *K14-Cre*, the XCI mosaic can be selectively visualized in adult cerebellar Purkinje neurons (Figure 1F) and in skin and hair follicles (Figure 1G), respectively. In the skin and cornea, contiguous patches of keratinocytes and endothelial cells express the same XCI reporter (Figures 1H and 1I). In the most superficial layers of the epidermis, where keratinocytes undergo programmed cell death, there is a loss of nuclear localization of the reporters. Many intestinal villi exhibit vertical stripes of GFP+ and tdT+ cells, reflecting the upward migration of clonal epithelial cells from the site of stem cell proliferation at the base of the crypts (Figure 1J). Skeletal muscle fibers, visualized using an *Mlc-Cre* transgene, show a range of colors intermediate between green and red, which presumably reflects the ratio of GFP+ to tdT+ myoblasts that fused to form each myotube, as seen in the flat-mounted diaphragm (Figure 1K). In the tongue musculature, a marked difference in color across the midline likely reflects the contributions of different ratios of GFP+:tdT+ progenitors from the left and right sides of the embryo (Figures 1L and 1M). In contrast to skeletal muscle, cardiac muscle (Figures 1N and 1O) and smooth muscle (Figure 1P) do not form by cell fusion and therefore do not exhibit colors intermediate between green and red. In cartilage, clusters of cells expressing the same XCI reporter show little intermingling, presumably due to the limited mobility of clonally derived progeny in the cartilage micro-environment (Figure 1Q). A flat-mount view of the organ of Corti shows fine-grained intermingling of GFP+ and tdT+ auditory hair cells and nonsensory epithelial cells (Figure 1R). In all adult tissues examined other than skeletal muscle, labeled nuclei were either GFP+ or tdT+, and none contained a mixture of the two reporters, consistent with the mutually exclusive nature of XCI.

Images from $Hprt^{GFP/tdT}$ females costained with DAPI reveal either GFP or tdT accumulation in every nucleus (data not shown), indicating that these knockin reporters are not subject to variegation. Therefore, the fidelity of reporter expression is limited only by the fidelity of *Cre* expression. This is in contrast to some transgenes and reporters (Ramírez et al., 2001).

In addition to the observed XCI variation within tissues, the overall [R/(R + G)] ratio varies widely between individuals, including littermates (Figures 1S and 1T). Interindividual XCI variation in the mouse is referable—at least in part—to allelic variation in the X chromosome controlling element (*Xce*) as well as other X-linked loci (Cattanach, 1975; Thorvaldsen et al., 2012).

In the next several sections, we analyze local, global, and interindividual differences in the topography of XCI mosaicism for a series of cell types within the CNS.

Quantitative Analysis of XCI Mosaicism among Cone Photoreceptors

As noted in the Introduction, the topography of XCI mosaicism among cone photoreceptors is of special interest. Using a

Figure 1. A Dual-Color Genetic System for Cell-Type-Selective Visualization of XCI Mosaicism

(A) Diagram showing Cre activation of the two reporters at the X-linked *Hprt* locus.

(B–R) Representative images showing XCI mosaicism in various tissues from females heterozygous for the *Hprt* reporters. In (F) (G) and (K–M) the mice carry $Hprt^{LSL\text{-}GFP/LSL\text{-}tdT}$ together with a tissue–specific *Cre* driver; all other panels are from $Hprt^{GFP/tdT}$ mice. Scale bars represent 50 um (P and R), 100 um (E, G, M, O, and Q), 200 um (B–D, F, and H–K), and 500 um (L and N).

(S and T) $Hprt^{GFP/tdT}$ females that are either siblings and half-siblings (S) or siblings (T) show variability in whole body [R/(R + G)] ratios. Stitching artifacts in the composite images account for minor intensity variation in a checkerboard pattern.

See also Table S1.

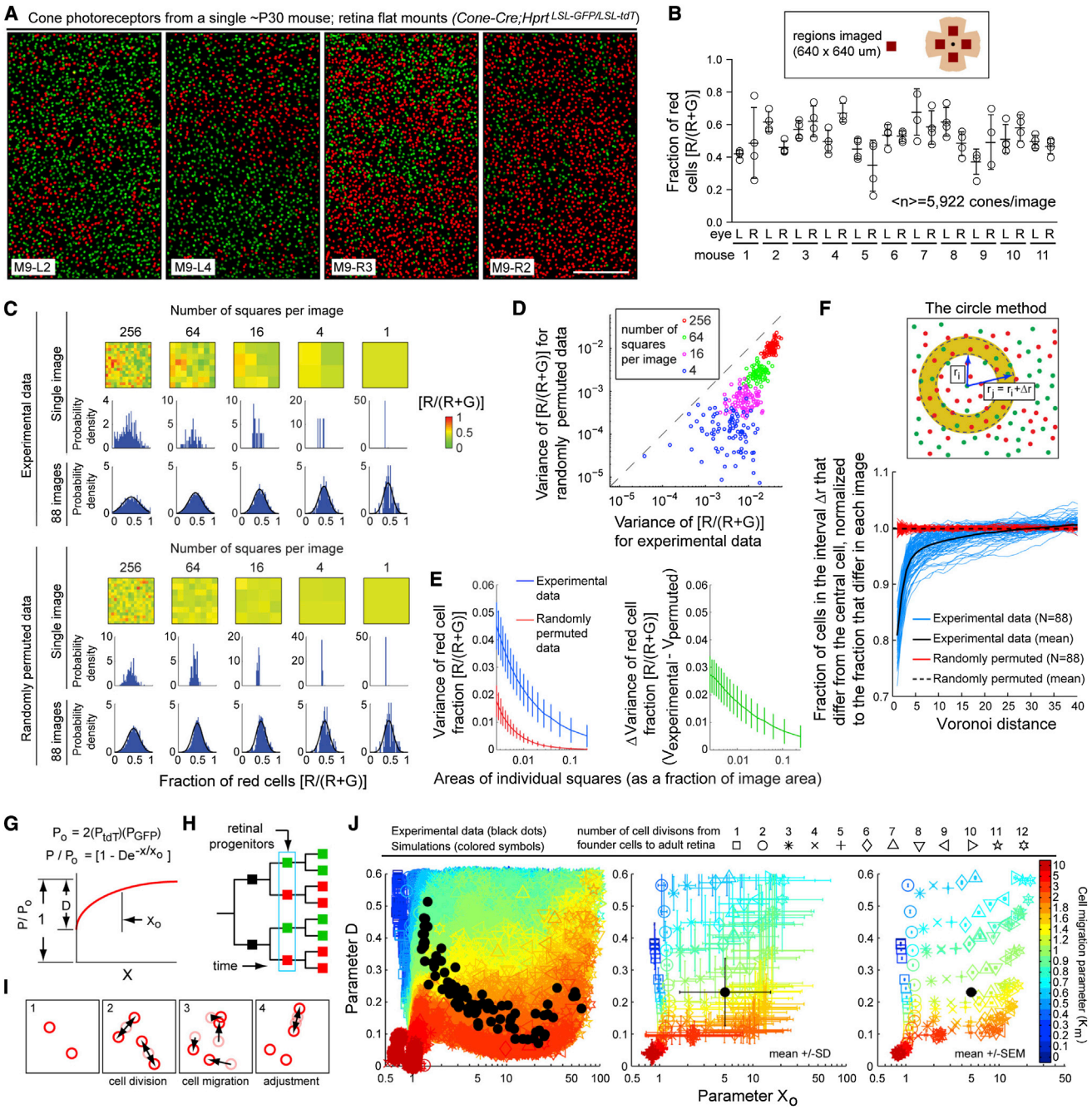

Figure 2. Quantitative Analysis of XCI Mosaicism among Cone Photoreceptors

(A) Cone photoreceptors in flat mounted retinas from four territories from a single *Cone-Cre;Hprt*$^{LSL\text{-}GFP/LSL\text{-}tdT}$ mouse. L, left retina; R, right retina. Scale bar represents 50 um.

(B) Top: schematic showing the four territories imaged per retina. Bottom: [R/(R + G)] ratios for cones in each territory. Comparing the mean [R/(R + G)] ratios for left versus right retinas, the correlation coefficient (*r*) = 0.26. Bars represent mean ± SD.

(C–E) The square method. (C) Subdivision of each 640 × 640 um territory into the indicated number of squares; [R/(R + G)] histogram for a single territory and for all 88 territories. The smooth curve shows a Gaussian with mean = 0.5 and variance matching each set of averaged data. Bottom, permuted control with cone locations unchanged but R versus G identities randomly permuted. For probability density histograms, x axis bin sizes are 0.02; the area under each curve is 1. (D) Variances of [R/(R + G)] for the experimental and randomly permuted data sets for each of the 88 territories with subdivisions at four spatial scales. (E) Left: means and SD of the 88 variances of [R/(R + G)] for experimental and randomly permuted data sets. The subdivisions are (starting from the far right): 4 squares/image, 9 squares/image, 16 squares/image, etc. Right: the difference between the two curves.

(F) The circle method. Top: schematic showing an annulus bounded by radii r_1 and r_2 and centered on one cone. For each cone, the fraction of the surrounding cells that differ in color from the central cell was determined for a contiguous series of annuli, and this value was normalized to the [R/(R + G)] ratio for that image.

(legend continued on next page)

cone photoreceptor-specific *Cre* transgene, we studied this topography in the adult retina (Figure 2). X-Y location and GFP+ versus tdT+ identity was determined for each cone in four 640 um × 640 um territories in both retinas from 11 *Cone-Cre;Hprt*$^{LSL\text{-}GFP/LSL\text{-}tdT}$ mice (4 × 2 × 11 = 88 territories; see Supplemental Experimental Procedures). A total of 521,161 cones were included in this analysis. By visual inspection, the cone XCI mosaic exhibits substantial inhomogeneity on a spatial scale of tens to hundreds of microns (Figure 2A). The fraction of red cones, [R/(R + G)], within each imaged territory ranged from 0.15 to 0.8, and within a single retina, the [R/(R + G)] ratios for different territories varied by as much as 0.5 (Figure 2B). Similar degrees of spatial inhomogeneity were observed in the XCI mosaics of several classes of amacrine cells and one class of retinal ganglion cells (Figure S1).

Two methods—referred to as "the square method" and "the circle method"—were used to quantify the magnitude and spatial scale of XCI inhomogeneity by assessing [R/(R + G)] ratios at different scales (see Supplemental Experimental Procedures). In the square method, each of the 88 territories was subdivided into grids of decreasing size and the [R/(R + G)] ratio was calculated for each subdivision (Figures 2C–2E). In the circle method (Rodieck, 1991), the [R/(R + G)] ratio was determined for cones located within a series of concentric annuli centered on each cone (Figure 2F). Control distributions for both methods were constructed by randomly permuting the GFP+ and tdT+ identities within each image.

Using the square method, Figure 2C shows histograms of [R/(R + G)] ratios for each of a series of progressively smaller subdivisions. The resulting probability density functions show that the inhomogeneity of the experimental data is greater than that of the randomly permuted data at every spatial scale. This differential was quantified by comparing the variances of the experimental and randomly permuted data for each of the 20 subdivision scales tested (including no subdivisions). As expected, the variances progressively increase with decreasing size of the subdivisions, but at every spatial scale the variance of the experimental data is greater than that of the randomly permuted data (Figures 2D and 2E). The circle method confirms the broad spatial scale of XCI inhomogeneity and further shows that within a Voronoi distance of ~5 cone territories (~30 um) the [R/(R + G)] ratio rapidly asymptotes toward the territory's mean ratio and between Voronoi distances of ~5 and ~25 cone territories (~30 um to ~150 um) there is a slower approach to the mean (Figure 2F). Of note, there is substantial variation between territories in the rate at which the [R/(R + G)] ratio asymptotes.

Spatial inhomogeneity in the adult XCI mosaic is governed by two factors: (1) the ratio of founder cells to adult cells (i.e., the number of cell divisions required to produce the adult structure), and (2) cell migration and intermixing during development. (Cell death is neglected for this analysis.) The retinal cone mosaic presents an especially attractive system for exploring these factors because the mosaic is confined to two dimensions and the number of cells that were scored is very large. Using the data set described above, a series of simulations were carried out for each of the 88 territories imaged. For these simulations, we systematically varied the number of progenitors (12 conditions) and the extent of cell migration (19 conditions) for a total of 12 × 19 = 228 conditions, and ran each condition 400 times (Figures 2H and 2I). The simulated XCI mosaics were analyzed using the circle method, and we then compared the simulated and experimental values of the circle method parameters D and X_0 that define the spatial scale of XCI inhomogeneity (Figures 2G and 2J). Within a plane defined by D and X_0, the 88 experimental data points sweep out a broad arc (black dots in J), and when compared to the simulated data the mean of the experimental data is centered at approximately six cell divisions and at a migration parameter of ~1.0, roughly the geometric midpoint of the range tested. However, the most striking aspect of this comparison is the large range of parameter values required to optimally fit all 88 experimental data points.

The XCI Mosaic in the Organ of Corti

Like the retina, the simple geometry and biological importance of the organ of Corti (OC) recommends it as a tissue in which to study the topography of XCI mosaicism. Using *Calb2-Cre;Hprt*$^{LSL\text{-}GFP/LSL\text{-}tdT}$ mice, in which reporter expression is activated in auditory hair cells, we analyzed 44 flat mounted P5 OCs, of which 42 represent paired left and right samples (Figures 3A and S2). From these images, 99,507 hair cells were scored for R versus G identity, X-Y position, and position within each of four rows (inner hair cell [IHC], outer hair cell row 1 [OHC-1], OHC-2, or OHC-3; see Supplemental Experimental Procedures). Substantial variation is observed in the [R/(R + G)] ratio for individual OCs, ranging from 0.1 to 0.9, with a mean ± SD of 0.45 ± 0.16 (Figures 3E and 3F). Approximately 70% of this [R/(R + G)] variation arises from interindividual differences in XCI mosaicism and ~30% reflects differences between left and right OCs within individuals (Figure 3F).

Using a one-dimensional analog of the two-dimensional circle method described above (see Supplemental Experimental Procedures), we observe almost no correlation in R versus G

Bottom: blue lines, mean [R/(R + G)] (normalized to 1.0 for each territory) as a function of distance for all cones in each territory. Red lines, cone identities randomly permuted.

(G–I) Modeling the development of the XCI mosaic with two degrees of freedom: number of founder cells and cell migration. (G) Circle method parameters D and X_0: for each cone, [R/(R + G)] asymptotically approaches a normalized value of 1.0, approximated by $P/P_0 = (1 - De^{-x/x0})$, where $P_0 = 2P_{tdT}P_{GFP}$ is the value of P at infinite distance. X = Voronoi distance. (H) The lineage model: the vertical arrow indicates the founder pool. (I) The four steps for each round of cell division: (1) starting configuration, (2) randomly oriented cell division, (3) cell migration, and (4) cell positions adjusted to avoid crowding.

(J) Comparison between observation and simulation. For each of the 88 images, simulations were performed with a [R/(R + G)] ratio in the progenitor pool that matched the observed ratio. The size of the simulated progenitor pool varied inversely with the number of cell divisions from founder cells to adult retina. Four hundred simulations were performed for each combination of founder cell number and migration rate, and the resulting mosaic of R and G cells was analyzed using the circle method to derive D and X_0 values. For each combination of founder cell number (symbol) and migration rate (color), the plots show individual D and X_0 values (left), mean and SD (center), and mean and SEM (right). Black dots, experimental data.

See also Figure S1 and Table S5.

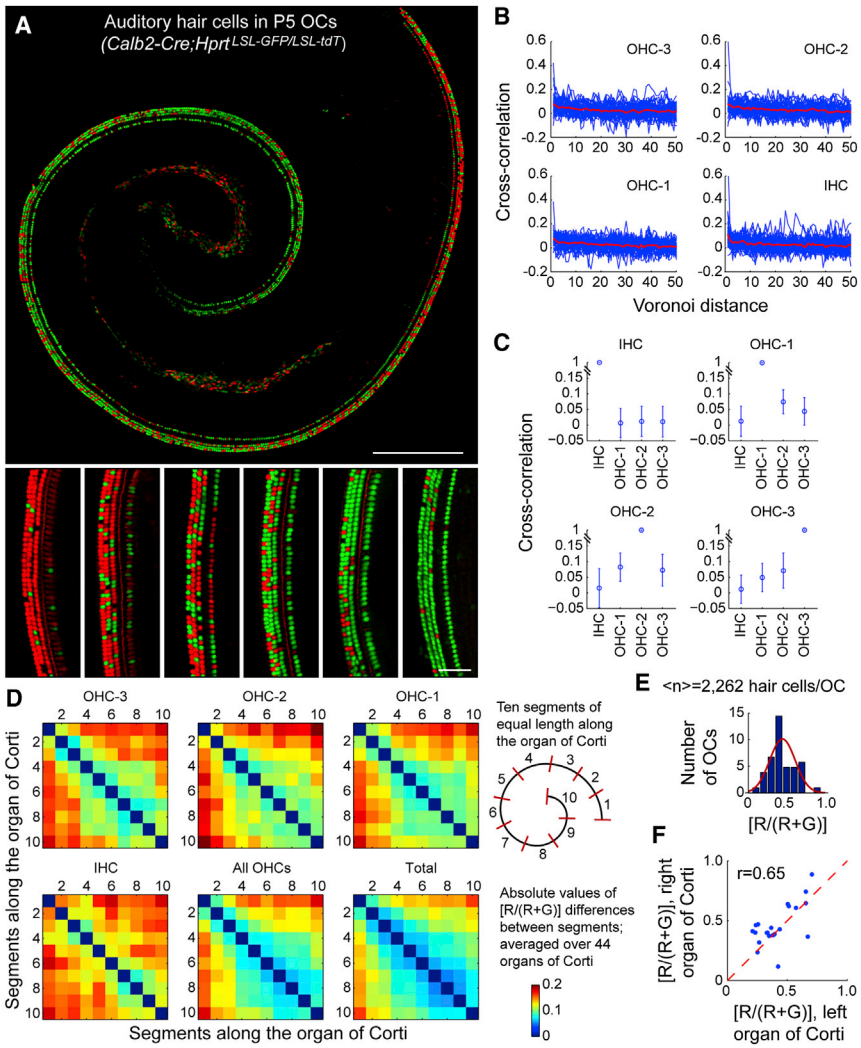

Figure 3. Regional and Interindividual Variation in XCI Mosaicism in the Organ of Corti

(A) Examples of flat-mounted P5 *Calb2-Cre;Hprt*$^{LSL\text{-}GFP/LSL\text{-}tdT}$ OCs illustrating the extent of XCI variability within a single OC (upper) and among OCs (lower). Occasional unlabeled hair cells likely reflect variegation of the Cre driver. Scale bars represent 300 um (upper) and 50 um (lower).

(B) Cross-correlations for R versus G identity within each of the four rows of hair cells determined with a one-dimensional version of the circle method, normalized for each row to the overall [R/(R + G)] ratio. Blue lines, cross-correlations for all hair cells in each of 44 P5 *Calb2-Cre;Hprt*$^{LSL\text{-}GFP/LSL\text{-}tdT}$ OCs. Red line, mean for the 44 OCs.

(C) Cross-correlations for R versus G identity among nearest neighbors across adjacent rows of hair cells, normalized to the [R/(R + G)] ratios of the two rows being compared. A value of 0 represents no correlation; 1.0 represents perfect correlation.

(D) Heatmaps quantifying pairwise differences in [R/(R + G)] ratio in 10% length intervals for hair cells from base to apex for the 44 OCs.

(E) [R/(R + G)] ratios for hair cells from 44 P5 *Calb2-Cre;Hprt*$^{LSL\text{-}GFP/LSL\text{-}tdT}$ OCs. Smooth line, best-fitting binomial distribution.

(F) [R/(R + G)] ratios for hair cells from 21 pairs of left and right P5 *Calb2-Cre;Hprt*$^{LSL\text{-}GFP/LSL\text{-}tdT}$ OCs. See also Figure S2.

identities between neighboring cells along each of the four rows of hair cells (Figure 3B). The R versus G correlation is also extremely low between nearest-neighbor cell pairs in adjacent rows of OHCs and is essentially zero between IHCs and OHCs (Figure 3C). These observations imply very thorough intermixing of nearby cells during development of the sensory epithelium. Intermixing appears to be less effective on a large scale, as changes in [R/(R + G)] ratio are apparent along the length of several OCs (Figures 3A, S2D, S2G, and S2H). To quantify this phenomenon, the ordered list of hair cells comprising each hair cell row in the 44 OCs was divided into tenths and the difference in [R/(R + G)] values was calculated for all pairs of subdivisions within each row. The mean of the absolute value of these differences is plotted in Figure 3D, which shows that, on average, there is a progressive decorrelation of [R/(R + G)] ratio with greater distance along the OC. These data are consistent with a model in which variation in the topography of XCI mosaicism along the OC reflects statistical fluctuations in a relatively small population of progenitors.

XCI Mosaicism in the Cerebral Cortex

The developing cerebral cortex exhibits two distinct patterns of neurogenesis. Excitatory neurons (pyramidal cells) are generated in the ventricular zone and migrate radially into the immediately overlying cortex (Parnavelas, 2000). By contrast, inhibitory interneurons are generated in the ganglionic eminences and undergo long-range tangential migrations to populate the entire cortex (Wonders and Anderson, 2006). Here, we ask how these proliferation and migration patterns affect the XCI mosaics for different types of cortical neurons. Because the cortical column, the fundamental unit of cortical information processing, encompasses a region of several hundred microns in diameter, there is a special interest in comparing this spatial scale to that of XCI mosaicism.

In the adult brain, excitatory neurons were visualized with *Camk2-Cre;Hprt*$^{LSL\text{-}GFP/LSL\text{-}tdT}$ mice (Figure 4A), and inhibitory GABAergic interneurons with *Gad2-Cre;Hprt*$^{LSL\text{-}GFP/LSL\text{-}tdT}$ mice. Additionally, a subpopulation of excitatory neurons—layer 4/5 cortical pyramidal cells—was visualized with a *Rbp4-Cre* driver, and three subpopulations of inhibitory interneurons were visualized with *Pv-Cre*, *Sst-Cre*, and *Vip-Cre* drivers (Figure 4A). For each genotype, six to nine 1 mm × 3 mm images were obtained from sagittal sections of cortex (Figure 4B) and GFP+ and tdT+ cells were scored manually (Figure 4A, central panels). Following the logic of the square method, each cortical

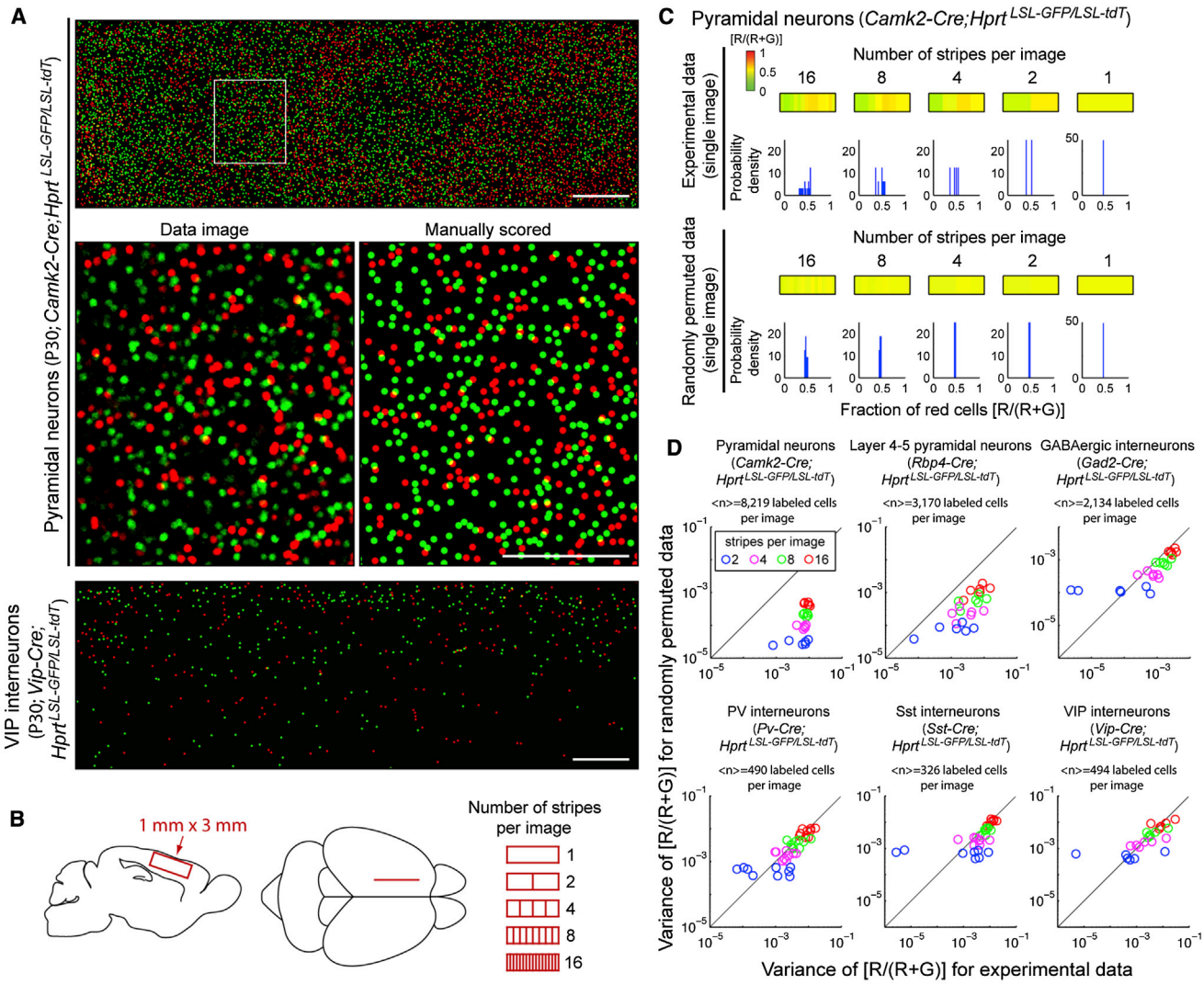

Figure 4. Cell-Type Differences in XCI Mosaicism in the Cerebral Cortex

(A) Pyramidal neurons (upper panels) and *Vip*-expressing interneurons (bottom panel) in 1 mm × 3 mm sagittal images of adult cerebral cortex. The inset in the upper panel is enlarged in the center left panel ("data image"); the manually scored version of the same image, in which each GFP+ or tdT+ nucleus is represented as a green or red disc, respectively, is at center right. Scale bars represent 300 um.

(B) Left: location of 1 mm × 3 mm sagittal images for cortical neuron quantification. Right: stripe method for dividing the images.

(C) The stripe method for analyzing XCI mosaicism illustrated with a single 1 mm × 3 mm *Camk2-Cre;Hprt*$^{LSL\text{-}GFP/LSL\text{-}tdT}$ image, subdivided along its long axis into the indicated number of stripes. Upper panels: experimental data. Lower panels: a control in which G versus R identities have been randomly permuted. For probability density histograms, x axis bin sizes are 0.02; the total area of the histogram is 1.

(D) Variances of the [R/(R + G)] distributions. Variance for experimental data versus the mean variance for 1,000 random permutations of R and G identity within each image. Each point represents a single 1 mm × 3 mm image, divided into the indicated number of stripes.

image was divided into a series of stripes as shown in Figure 4B and the [R/(R + G)] ratio was determined for each stripe (Figure 4C). As a control, 1,000 random permutations of R versus G identities were performed for each image.

By visual inspection, each of the labeled neuronal populations shows substantial intermingling of GFP+ and tdT+ cells. However, a comparison of the variances of the experimental and permuted data reveals a striking difference between pyramidal and interneuron populations (Figure 4D). For pyramidal neurons, the mean variance of the experimental data is ~10-fold (*Rbp4*-expressing neurons) or ~100-fold (*Camk2*-expressing neurons) larger than the mean variance of the permuted controls, and this difference in variances is apparent on all spatial scales examined. The largest spatial scales (e.g., dividing the 1 mm × 3 mm image into 2, 4, 8, or 16 stripes) encompass the scale of cortical columns (in the mouse barrel cortex, individual barrels have diameters of 150–300 um; Jan et al., 2008). This heterogeneity of XCI mosaicism most likely

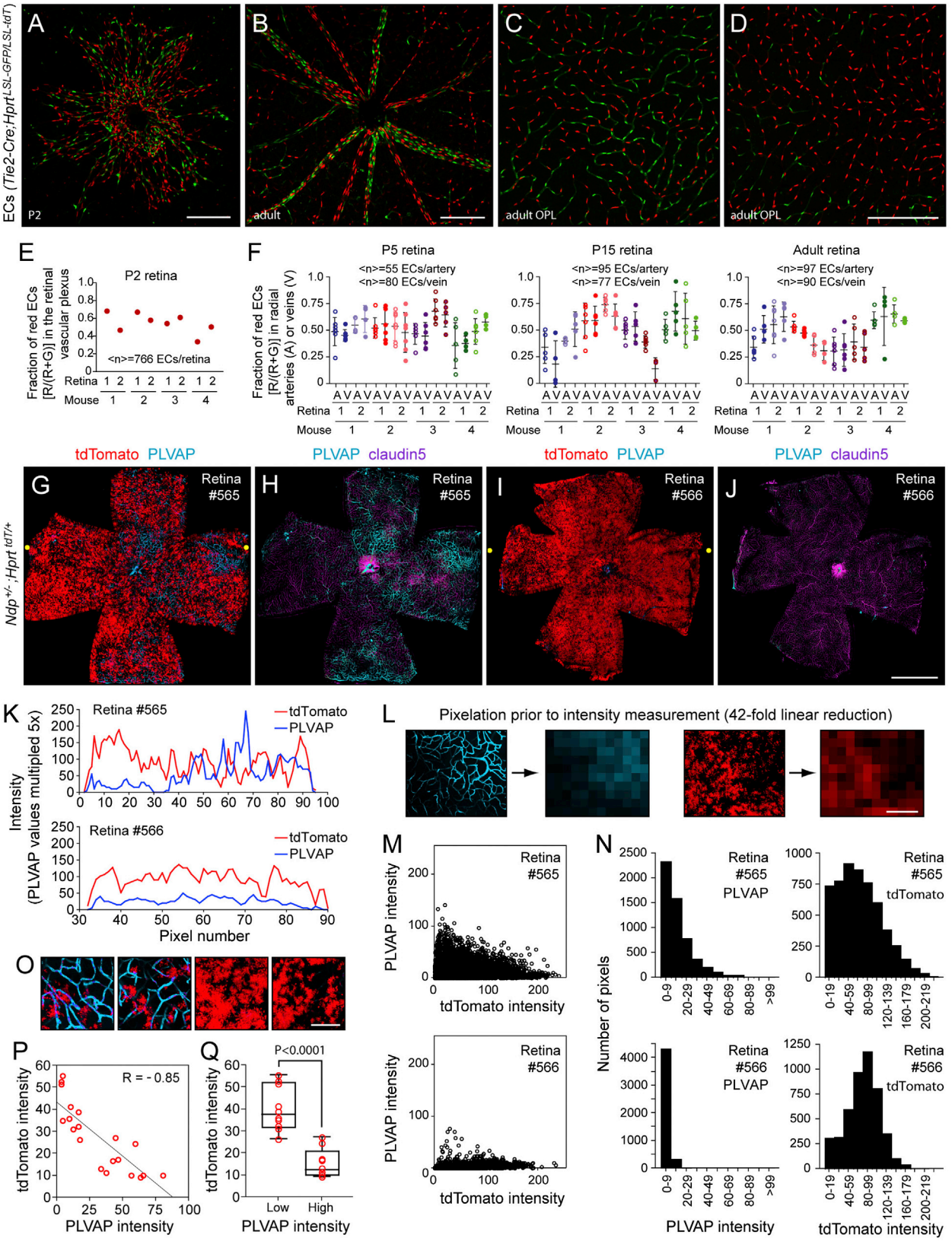

(legend on next page)

reflects the coarse-grained division of the neural tube into zones of clonally related progenitors (described below) and the limited tangential migration of pyramidal neurons from their origin in the ventricular zone (Tan et al., 1998). By contrast, all four interneuron types show roughly the same mean variances for experimental and randomly permuted data (Figure 4D). Apparently, interneurons become finely intermixed during proliferation in the ganglionic eminences and/or during tangential migration across the cortex.

XCI Mosaicism in CNS Vasculature

Vascular endothelial cells (ECs) invade the developing neural tube beginning at ~E9.5 (Stenman et al., 2008) and they spread radially across the developing retina from the optic disc beginning at ~P0 (Fruttiger, 2007). In both tissues, relatively small numbers of ECs invade their targets and then proliferate in situ, an angiogenic sequence that should favor spatial inhomogeneity in the vascular XCI mosaic. Countering the propensity toward local clonality is the high mobility of developing ECs (Jakobsson et al., 2010).

To visualize the XCI mosaic among vascular ECs, we examined brain sections and retina flatmounts in *Tie2-Cre;Hprt*$^{LSL\text{-}GFP/LSL\text{-}tdT}$ mice. In a set of eight P2 retinas, the [R/(R + G)] ratio for the entire vascular plexus ranged from 0.3 to 0.7 (Figures 5A and 5E). In P5, P15, and adult retinas, the [R/(R + G)] ratio for single radial arteries and veins generally clustered within ±0.2 of the mean for an individual retina, and across the population surveyed, these ratios varied from <0.1 to ~0.9 (Figures 5B and 5F). Capillaries within the outer plexiform layer (OPL) showed substantial region-to-region variation in [R/(R + G)] ratio as seen in comparing Figures 5C and 5D. In each of four adult brains, we counted GFP+ and tdT+ ECs in four territories within coronal sections of the cerebral cortex, two in each hemisphere, with ~8,000 ECs per territory (data not shown). One brain showed minimal variability, with the four [R/(R + G)] ratios clustered near the mean of 0.7. By contrast, the [R/(R + G)] ratios in the three other brains varied over a range of ~0.5 for each brain. These data suggest that X-linked variation that produces a cell autonomous EC phenotype could generate region-to-region variability in heterozygous females.

Effects of XCI Mosaicism in a Mouse Model of the Norrie Disease Carrier State

Correlating XCI mosaicism with cellular and/or physiological defects in mouse models of X-linked disease can reveal determinants of clinical phenotype in female carriers, as demonstrated here for Norrie disease, an X-linked disorder in which mutations in *NDP*, the gene coding for a glial-derived ligand (Norrin), lead to defects in retinal vascular proliferation, tissue invasion, and barrier formation (for review, see Berger and Ropers, 2001; Ye et al., 2010). The Norrin receptor, Frizzled4 (Fz4), is constitutively expressed by vascular ECs, which respond to Norrin-Fz4 binding by activating canonical Wnt signaling. Clinical case reports document variable manifestations of retinal vascular defects among women who are obligate Norrie disease carriers (Sims et al., 1997; Lin et al., 2010).

To explore the factors that are relevant to the vascular phenotype in Norrie disease carriers, we analyzed vascular structure and XCI mosaicism in retinal flatmounts from three young adult female *Ndp*$^{+/-}$;*Hprt*$^{tdT/+}$ mice. In these mice, the *Ndp*$^{-}$ and *Hprt*^{tdT} alleles reside on different X chromosomes, and therefore tdT+ and tdT− territories correspond to *Ndp*$^{+}$ and *Ndp*$^{-}$ territories, respectively. In contrast to the severe defect in vascularization seen in *Ndp*$^{-/-}$ female and *Ndp*$^{-/Y}$ male mice, *Ndp*$^{+/-}$ females show only a modest reduction in vascular density in the inner and outer plexiform layers. However, the blood-retina barrier appears to be highly sensitive to spatial variation in Norrin production, as assessed by induction of plasmalemma vesicle-associated protein (PLVAP), a structural component of the endothelial fenestrations that demarcate ECs that have lost barrier function (Wang et al., 2012) (Figures 5G–5N). Retinas with relatively coarse-grained XCI mosaicism show PLVAP+ vessels with a spatial distribution that closely matches the distribution of cells expressing the *Ndp*$^{-}$ X chromosome (Figures 5G and 5H; retina #565), whereas retinas with finer-grained XCI mosaicism and a higher fraction of retinal cells expressing the *Ndp*$^{+}$ allele show minimal PLVAP expression (Figures 5I and 5J; retina #566).

Several procedures served to quantify the relationship between the spatial distributions of tdT+ versus tdT− tissue and PLVAP+ versus PLVAP− vasculature. First, to average tdT and PLVAP intensities over a spatial scale of hundreds of microns,

Figure 5. XCI Mosaicism in Retinal Vascular Development and in a Mouse Model of the Norrie Disease Carrier State

(A–D) P2 and adult retina flat mounts. Heterogeneity is observed in [R/(R + G)] ratio in radial vessels (B) and in outer plexiform layer (OPL) capillaries (C and D). Scale bars represent 200 um.

(E and F) Quantification of [R/(R + G)] ratios in retinal vasculature for four mice (eight retinas) at P2, P5, P15, and adulthood. For P5 to adulthood, only vessels with >25 ECs were included.

(G–J) P22 female *Ndp*$^{+/-}$;*Hprt*$^{tdT/+}$ retina flatmounts immunostained for PLVAP and claudin5; the z stack images encompass only the inner and outer plexiform layer capillary beds to avoid inhomogeneities from superficial veins and arteries. Retina #565 exhibits coarse-grained XCI mosaicism and multiple PLVAP+ territories. Retina #566 (from a different mouse) has a higher fraction of WT (tdT+) cells and finer-grained XCI mosaicism. Scale bar represents 1 mm.

(K and L) Images were reduced from ~4,200 × 4,000 pixels to 100 × 95 pixels (L). The tdT and PLVAP intensities from a single horizontal row of pixels [location marked by yellow dots in (G) and (I)] are plotted in (K). Scale bar in (L) represents 200 um.

(M and N) tdT and PLVAP intensities from 100 × 95 pixel images. Compared to retina #566, retina #565 shows a broader distribution of tdT intensities (N, right two panels), implying more variability in the XCI mosaic at this spatial scale, and a broader range of PLVAP intensities (N, left two panels). tdT and PLVAP intensity distributions are anticorrelated (M).

(O–Q) The 5.88 mm × 5.6 mm image of retina #565 was divided into squares of 280 um × 280 um, from which ten squares with average PLVAP intensities <20 and ten squares with PLVAP intensities >30 were selected at random. (O) Two examples of each category. Average tdT and PLVAP intensities for the 20 squares are plotted in (P) and (Q). The box and whisker plots in (Q) mark the median, the 25th and 75th percentiles, and the extremes. P value, nonpaired Student's t test. Scale bar in (O) represents 100 um.

the retina flat mount images were reduced from ~4,200 × 4,000 pixels to 100 × 95 pixels and the tdT and PLVAP intensities were plotted for individual rows of pixels, revealing a rough anticorrelation of the two distributions (Figures 5K and 5L). Second, using the same pixelated data set to generate scatter plots and histograms of tdT and PLVAP intensities, retina #565 showed a broad distribution of tdT and PLVAP intensities and an anticorrelation of the two distributions, whereas retina #566 showed a relatively narrow distribution of tdT intensities with little PLVAP signal (Figures 5M and 5N). Third, the image of retina #565 was divided into 420 squares (21 × 20) and the mean tdT intensities were determined for ten squares with high mean PLVAP intensity and for ten squares with low mean PLVAP intensity, the 20 individual squares having been selected at random from within their respective subgroups (Figure 5O). In this data set, tdT and PLVAP intensities strongly anticorrelate and the two subsets of tdT intensities differ with $p < 0.0001$ (Figures 5P and 5Q).

The interesting inferences from this analysis are that (1) Norrin diffusion appears to be highly restricted in vivo, (2) retinal ECs do not maintain a barrier state if they are not exposed to nearly WT levels of Norrin, and (3) variation in the topography of XCI mosaicism is sufficiently great in the mouse retina to reveal the effects of the first two factors in a subset of eyes. The variability in clinical manifestations seen in human carriers of *NDP* mutations could plausibly reflect these same factors.

Left-Right Asymmetry

In surveying XCI mosaicism in paired left and right structures such as the retina and OC, or in bilaterally symmetric structures that straddle the midline such as the tongue and vasculature, we frequently observed substantial left-right asymmetries. For example, 3/5 tongues show clear [R/(R + G)] differences between the left and right sides (Figure 1L), 2/11 retinas show no overlap in the four sets of left versus right [R/(R + G)] cone counts (Figure 2B), and 6/21 pairs of left and right cochlea show a [R/(R + G)] ratio difference >0.2 (Figure 3F). Left-right asymmetry in CNS structure and function has been studied extensively, but its biological basis remains obscure (Sperry, 1982; Levin, 2005).

To explore the extent to which XCI mosaicism might contribute stochastically to left/right asymmetry, we began by characterizing XCI mosaicism in the neural tube. At E11.5, the $Hprt^{GFP/tdT}$ neural tube exhibits irregular green and red territories with essentially no correlation in XCI topography between left and right sides (Figures 6A–6D). The correlation coefficient of the mean [G/(G + R)] ratio between left and right sides of the neural tube is 0.187. To explore left/right and interindividual XCI variation more broadly, we surveyed additional CNS structures and cell types. Hypothalamic *Pomc*-expressing, *Lepr*-expressing, and *Crh*-expressing neurons show left-right [R/(R + G)] differences in individual coronal sections and interindividual differences (averaged over multiple sections) of up to ~0.2 (Figures 6E, S3C, and S3D). *Th*-expressing neurons in the ventral tegmental area and substantia nigra show a similar pattern, with interindividual [R/(R + G)] differences (averaged over multiple coronal sections) of up to ~0.3 (Figures S3A and S3B). These analyses also show [R/(R + G)] variation of up to ~0.3 for different rostrocaudal positions within an individual brain, likely reflecting [R/(R + G)] variation along the length of developing neural tube (Figures S3A and S3B). In a survey of XCI in multiple anterior pituitary cell types, interindividual [R/(R + G)] differences ranged up to ~0.3 (Figure S4). Among spinal motor neurons, variation in the [R/(R + G)] ratio between left and right sides and along the neuraxis is relatively large (Figure 6E), reflecting statistical fluctuations among motor neuron progenitors and the small number of adult motor neurons per section.

In keeping with the quantification of [R/(R + G)] ratios for specific retinal cell types (Figures 2 and S1), large variations are seen in [R/(R + G)] ratios between developing left and right eye cups and adult retinas when all cell types are labeled (Figures 6F and 6G). As for the spinal cord, these variations most likely reflect the small number and limited migration of progenitors.

Finally, in surveying serial coronal sections of E13, E14, and adult brains in which pyramidal neurons were visualized with *Emx1-Cre* or *Camk2-Cre*, we observed 5/16 brains with left-right [R/(R + G)] ratio differences that encompassed a large fraction of each hemisphere as shown in Figure 6H. As suggested above for variation among spinal motor neurons, these large-scale variations likely reflect statistical fluctuations in [R/(R + G)] ratio among progenitors in the midgestation neural tube as seen in Figures 6A and 6B.

In Mice, Very Few X-Linked Genes Escape XCI

The availability of mouse lines expressing an X chromosome-encoded fluorescent reporter presents an opportunity to physically purify cells based on XCI status and to use the purified cells to define XCI status for all active genes in that population. This experiment is of interest because previous surveys of XCI in mice using various cell lines showed that a far lower percentage of mouse genes partially or completely escape XCI (~3%; Yang et al., 2010; Li et al., 2012; Pinter et al., 2012) compared to the percentage observed in primary human fibroblast cell lines (~15%; Carrel and Willard, 2005). As patterns of gene expression in cell lines can reflect selective pressures related to growth in vitro, it would be desirable to extend the analysis of XCI to cells obtained directly from a living mouse.

For this experiment, we crossed female *M. castaneous* to male *M. musculus* ($Hprt^{tdT}$) and male *M. castaneous* to female *M. musculus* ($Hprt^{tdT/tdT}$). From individual P0 female progeny carrying $Hprt^{tdT}$ on the *M. musculus* X chromosome, brain cells were separated by FACS into tdT+ and tdT− populations (Figures 7A and S5). Transcripts from the four cell populations were analyzed by RNA-seq and were found to encompass 55,462 previously defined SNPs that distinguish the *M. musculus* and *M. castaneous* genomes, of which 1,232 reside on the X chromosome (Tables S2 and S3). For this analysis, we have included only those SNPs for which we observed greater than ten reads. The upper panels of Figure 7B shows the number of reads for each SNP for all X chromosome SNPs and for an equal number of autosomal SNPs (from chromosome 11). The lower panels of Figure 7B show SNP read counts for nine genes, representing the six major classes of epigenetic regulation: (1) autosomal, not imprinted, (2) autosomal, maternally imprinted, (3) autosomal, paternally imprinted, (4) X-linked and obeying

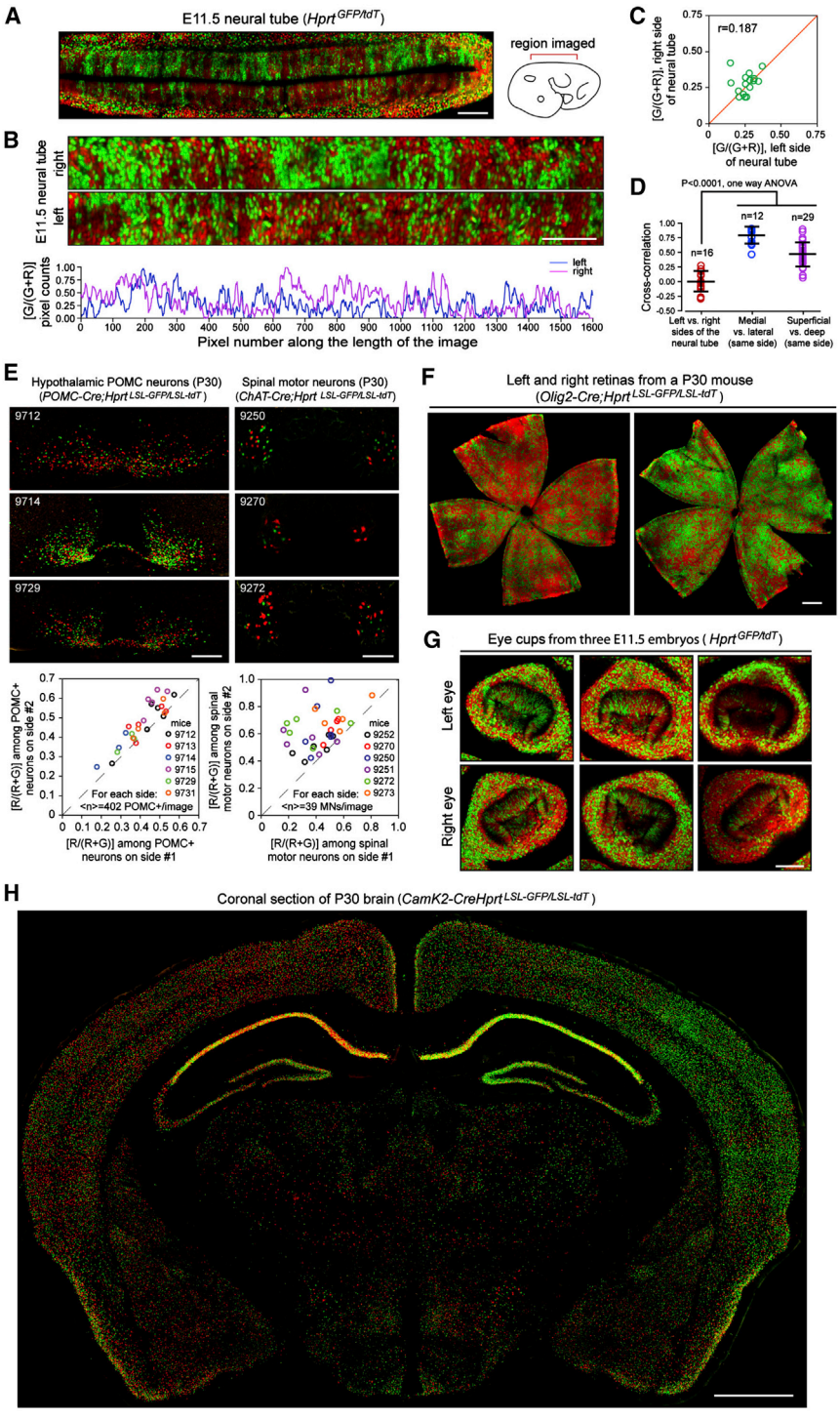

Figure 6. Left-Right Asymmetry in XCI Mosaicism

(A) E11.5 *Hprt*$^{tdT/GFP}$ embryo, dorsal view of neural tube. Scale bar represents 200 um.

(B) Dorsal view and quantification of [G/(G + R)] pixel counts along the A-P axis for left and right sides of an E11.5 *Hprt*$^{tdT/GFP}$ neural tube. Scale bar represents 100 um. Anterior is at the left for (A) and (B).

(C) Mean [G/(G + R)] pixel counts in left versus right sides of 16 E11.5 neural tubes, as quantified in (B).

(D) Cross-correlations between [G/(G + R)] pixel counts along left versus right sides of 16 E11.5 neural tubes (as shown in B); mean correlation is zero. Control comparisons are between images from the same side of the neural tube but differing in lateral position by 20%, 40%, and 60% of their widths or in depth by 6 um and 12 um. The high cross-correlation in the control comparisons imply that small changes in image location would have only a modest effect on the left-right cross-correlation.

(E) XCI mosaicism among POMC neurons (left) and spinal motor neurons (right) in coronal sections of adult hypothalamus and spinal cord, respectively. Upper panels: representative sections. Lower panels: quantification of [R/(R + G)] ratios determined separately for left and right sides from three to seven coronal sections for each of six mice. By convention, the side with the larger [R/(R + G)] ratio is plotted on the y axis. Scale bars represent 200 um.

(F) Variation in XCI mosaicism in left versus right retinas in a single adult mouse. Scale bar represents 500 um.

(G) Variation in XCI topography in left and right eye-cups in three E11.5 embryos. Scale bar represents 100 um.

(H) XCI mosaicism in an adult brain shows left/right asymmetry among excitatory neurons in the cortex and hippocampus. In this figure and in all other images of adult cells other than skeletal muscle, GFP and tdT expression is mutually exclusive. The rare nucleus that appears yellow reflects the superposition of two differently colored nuclei in different z planes. Scale bar represents 1 mm.

XCI, (5) X-linked and expressed from the inactive X chromosome (*Xist*), and (6) X-linked and showing (partial) escape from XCI. A full list of maternally and paternally imprinted autosomal genes can be found in Table S2.

Among 263 X-linked transcripts that encompass one or more SNPs and were sequenced to sufficiently high coverage, 256 obey XCI. The remaining seven transcripts (*Ddx3x*, *Eif2s3x*, *Itm2a*, *Kdm5c*, *Kdm6a*, *Mid1*, and *5530601H04*) exhibit partial escape from XCI, and are dispersed along the X chromosome (Table S3). This set substantially overlaps the XCI escapee gene sets defined by RNA-seq using either an embryonic kidney cell line (Yang et al., 2010) or four neural stem cell lines (Li et al., 2012) and by ChIP-seq of repressive chromatin marks using ES cell lines and mouse embryo fibroblasts (Pinter et al., 2012). Some of the differences between these data sets likely arise from differences in cell type- and/or developmental stage-specific gene expression leading to insufficient RNA-seq

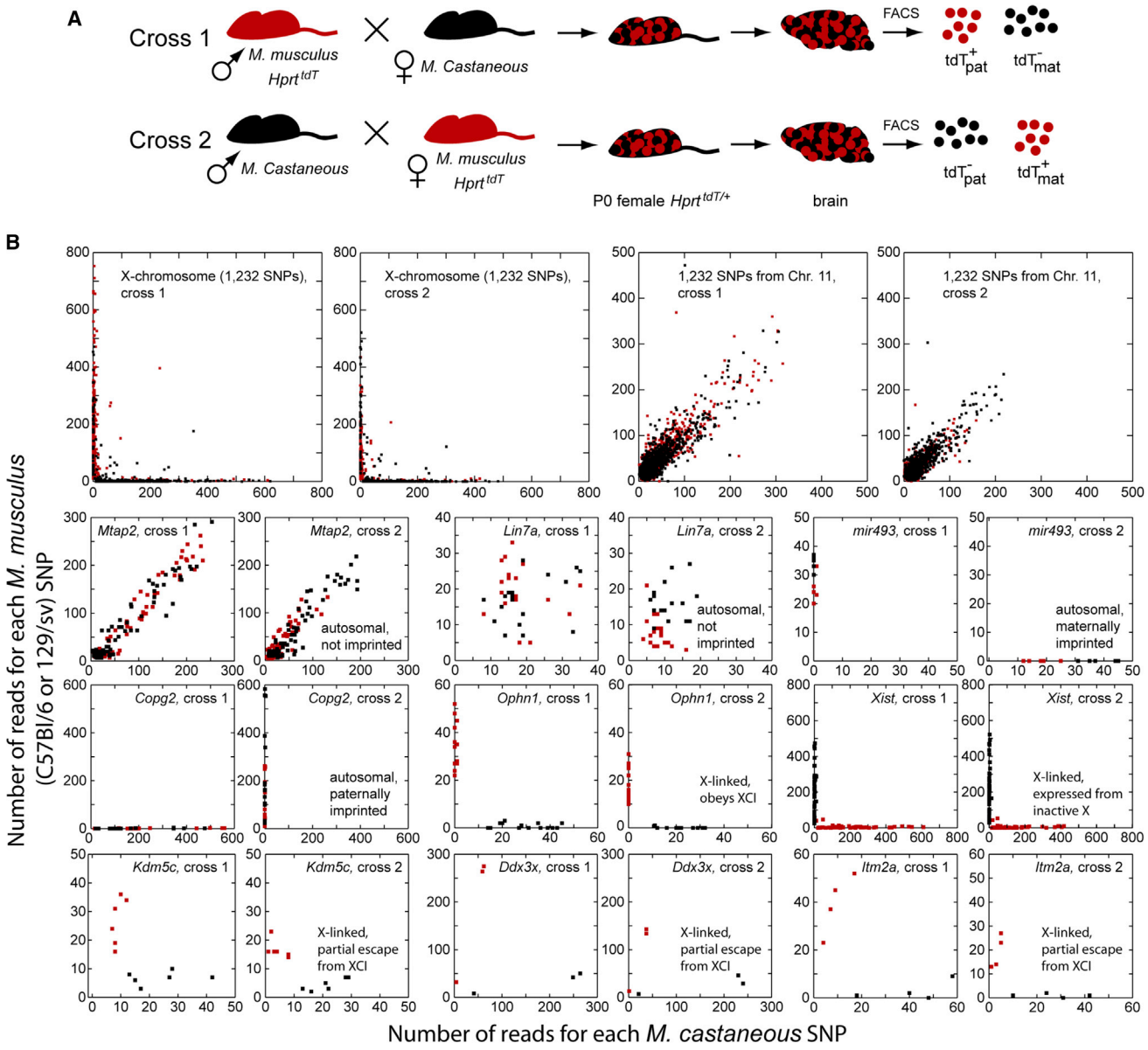

Figure 7. RNA-seq Identifies Genes Subject to or Partially Escaping XCI in the Early Postnatal Mouse Brain

(A) Reciprocal crosses between *M. musculus* and *M. castaneous*. FACS purification of dissociated P0 brain cells from $Hprt^{tdT/+}$ female progeny: four populations were purified for RNA-seq. Subscripts "pat" or "mat" refer, respectively, to the paternal or maternal origin of the $Hprt^{tdT}$ allele.

(B) Scatter plots showing the number of RNA-seq reads per SNP from the four cell populations shown in (A). Each pair of adjacent scatter plots shows SNP data from cross 1 (left plot) and cross 2 (right plot). Red and black symbols represent reads from tdT+ and tdT− cells, respectively. Upper row: all X chromosome SNPs (left) and an equal number of autosomal SNPs (right). Lower three rows: SNP data from nine genes illustrating the principal patterns of epigenetic regulation. In these plots, black symbols have been overlaid on red ones.

See also Figure S5 and Tables S2 and S3.

coverage in one or more data sets. As a technical aside, we note that the number of *M. castaneous* versus *M. musculus* SNP reads for genes that obey XCI indicates >98% purity of the cell populations (Tables S2 and S3). In sum, these data confirm and extend earlier results obtained with mouse cell lines and they stand in contrast to the observation of more widespread escape from XCI in humans.

In Humans, Polymorphic Coding Region Variants Occur at Similar Frequencies among X-Linked and Autosomal Genes

Extension of the present work to humans is hampered by the technical challenge of scoring XCI in postmortem brain tissue and purifying cells based on XCI status. However, there is one aspect of X chromosome variation that can be studied to greater

effect in humans than in mice: allelic variation in the natural population, which serves as the essential basis of all XCI-dependent phenotypic variation. To assess the extent of this variation, and, in particular, the frequency of common variants, we cataloged the number and frequency of all missense variants with a minor allele frequency (MAF) of >0.1 on the X chromosome and on a comparably sized autosome (chromosome 10) in the 1000 Genomes Project data set (Abecasis et al., 2012). This analysis reveals a modest elevation (~25%) in the frequency of missense variants with MAF >0.1 per gene on chromosome 10 compared to the X chromosome (Figure S6C). Among the 13 ethnic groups surveyed, the frequency of missense variants, mean MAF values, and identities of variants are similar (Figures S6A, S6B, and S6D). These data argue that purifying selection has not greatly reduced the frequencies of common coding variants on the X chromosome relative to their frequencies on autosomes. These common coding variants, together with the far larger number of rare coding variants (Fu et al., 2013), produce, on average, many allelic differences between any pair of human X chromosomes.

DISCUSSION

The Cre-activated dual-color reporter system described here represents the latest technical advance in a 50-year quest to define the topography of XCI mosaicism. Several experimental limitations of the earlier histochemical and genetically engineered reporter systems—including an inability to direct expression to defined cell types, the absence of distinct markers for the two X chromosomes, and, for histochemical reporters, incompatibility of the histochemical readout with confocal microscopy—have now been resolved with the development of Cre-activated nuclear-localized GFP and tdT reporters. We anticipate a variety of uses for this system. These include monitoring the development of XCI in living embryos, analyzing mouse mutants or cultured cells with perturbations in XCI, and visualizing or purifying defined cell types from female mice that are heterozygous for X-linked disease mutations to assess changes in gene expression, chromatin state, cell morphology, or cell physiology that distinguish WT and mutant cells.

XCI as a Generator of Cellular Diversity

We have shown here that XCI efficiently generates biological diversity both within and between individuals. In the former case, diversity is observed on spatial scales that span the range from individual cells to whole organs.

With respect to XCI variability within an individual, inhomogeneities in the XCI mosaic in any particular tissue reflect the interplay of two factors: (1) the ratio of founder cells to adult cells, and (2) the timing and extent of cell migration during development. Following this line of reasoning, the observed variation in [R/(R + G)] ratio along the length of the OC and between left and right OCs suggests that the OC is derived from a relatively small number of founder cells. In the retina, previous cell marking studies have precisely defined the patterns of cell proliferation and radial versus tangential migration after eye cup formation (Fekete et al., 1994; Reese et al., 1999). The topography of retinal XCI quantified here extends those observations by revealing XCI variation on spatial scales from neighboring cells to entire retinas. Substantial variation in the XCI mosaic is also seen in the retinal vasculature, where individual arteries and veins likely derive from a small number of ECs.

Another aspect of XCI mosaicism that is relevant to its role in CNS diversity is the cell-type dependence of XCI topography. In the cerebral cortex, the fine-grained intermixing of inhibitory interneurons predicts that heterozygosity for an X-linked gene that affects interneuron function will produce a relatively uniform perturbation of all cortical circuits. By contrast, the spatial heterogeneity of the XCI mosaic among excitatory neurons implies that heterozygosity for an X-linked gene that affects excitatory neuron function will likely result in column-to-column, region-to-region, and, in some individuals, left versus right differences in cortical function.

A different type of large-scale variation in XCI mosaicism in the mouse brain was reported by Gregg et al. (2010), who used an X-linked *GFP* transgene that exhibits cell type-restricted expression to quantify GFP+ cells in heterozygous female progeny with maternal versus paternal inheritance of the transgene. Gregg et al. observed 40%–50% more GFP+ cells in the cortex of mice that received the *GFP* transgene from the mother compared to the father, but there was no parent-of-origin effect in subcortical structures. We note that there are technical challenges inherent in the experimental design employed by Gregg et al. that could be overcome with the dual-color reporter system. Advantages of the dual color system include: (1) knockin reporter alleles that are not subject to variegation, (2) quantification based on the relative abundance of two differentially marked cell populations within the same image, and (3) nuclear-localization of the reporters. Although the difference between subcortical and cortical cell counts reported by Gregg et al. (2010) argues in favor of a parent-of-origin effect, our observation of frequent, large-scale, and apparently stochastic variation in XCI mosaicism within individual brains and between littermates argues for a cautious interpretation.

The similarities in early brain development across mammals (Molnár and Clowry, 2012) suggests that the observations made here with mice may also apply to humans. If this extrapolation is valid, it suggests that XCI mosaicism in the human CNS could generate stochastic, female-specific, functional diversity on diverse spatial scales. Although data on spatial patterns of XCI mosaicism in human solid tissues are limited, several examples, including ophthalmoscopic visualizing of RPE depigmentation in ocular albinism and choroideremia carriers, have revealed clear inhomogeneities in the XCI mosaic (Chung et al., 1998; Cohn et al., 1989; Coussa and Traboulsi, 2012). Because polymorphic variation on the human X chromosome appears to be widespread, XCI mosaicism may represent a significant source of "normal" person-to-person and region-to-region variation in CNS function, including left versus right brain asymmetry.

As noted in the Results section, interindividual XCI variation in the mouse derives, at least in part, from allelic variation in *Xce* and other X-linked loci. Given the wide range in [R/(R + G)] ratios that we observe among littermates, we speculate that additional mechanisms might contribute to variation in XCI. For example, among the gametes of a single individual, X chromosomes might carry epigenetic marks that produce an XCI bias for or against

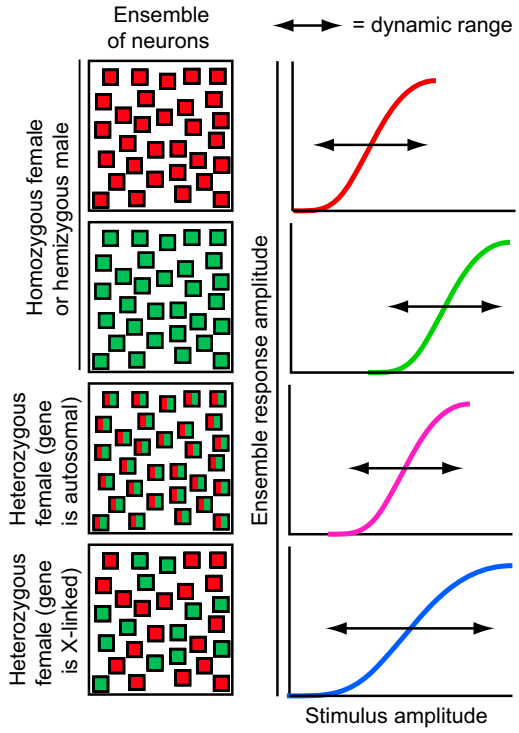

Figure 8. Model of Stimulus-Response Characteristics for Neural Circuits in Females Homozygous or Heterozygous for Allelic Variation

Left: squares represent individual neurons within a neural circuit, and red and green colors represent the gene products encoded by a pair of functionally distinct alleles. Right: stimulus-response properties for the neural circuit. The same dynamic range is predicted for the two classes of homozygotes (upper two panels) or, if the gene of interest resides on an autosome, for heterozygotes (third panel), because in each case the neural circuit is homogeneous with respect to production of the gene product of interest. However, if the gene of interest resides on the X chromosome, a larger dynamic range is predicted for heterozygous females because XCI mosaicism would create a neural circuit that consists of two biochemically distinct classes of cells.

the marked chromosome, and the presence of these marks might vary. A second possibility is that epigenetic marks that bias XCI might be acquired when the number of cells in an embryo is extremely small, leading to large fluctuations in XCI within the embryo. With respect to the contribution of XCI variation to human diversity, a survey of peripheral blood lymphocytes among 1,000 females demonstrated skewed XCI in a large proportion of phenotypically normal females, with 4.9% of newborns and 14.2% of adults exhibiting skewing greater than 80:20 (Amos-Landgraf et al., 2006). Some fraction of this skewing could reflect heterozygosity for alleles that impair cell proliferation or survival.

XCI Mosaicism and the Expression of X-Linked Traits

The XCI variability observed in mice and humans has important implications for variable expressivity of X-linked diseases in carrier females. For tissues or organs such as liver, kidney, and lung in which many cells perform essentially the same function, spatial inhomogeneity in the XCI mosaic should be of little phenotypic consequence. For these organs, the overall ratio of mutant:WT cells is likely to be the sole determinant of physiologic function, with the threshold for dysfunction set at different mutant:WT ratios depending on the disease and tissue (Dobyns et al., 2004). However, for tissues such as the retina or OC, in which distinct functions are spatially segregated—in these instances, detection of stimuli with different locations in visual space or different frequencies, respectively—XCI inhomogeneity could produce uncompensated phenotypes. Clinical observations are in general agreement with this prediction, as female carriers of X-linked retinitis pigmentosa gene mutations have variable vision loss (Grover et al., 2000) and female carriers of X-linked phosphoribosyl pyrophosphate synthetase I mutations (DFN2) or type IV collagen mutations (Alport syndrome) have variable hearing loss (Jais et al., 2003; Liu et al., 2010, 2013). Clinical manifestations are also variably present in female carriers of other X-linked neurologic diseases, including fragile X-associated tremor/ataxia syndrome (Chonchaiya et al., 2010; Tassone et al., 2012) and adrenoleukodystrophy (Jangouk et al., 2012).

Norrie disease results from a defect in a secreted polypeptide (Norrin), and, one might have predicted that diffusion of extracellular Norrin would produce a spatially homogeneous retinal phenotype in female carriers. Indeed, earlier experiments in which high level transgenic expression of Norrin from a lens crystallin promoter was observed to fully rescue the *Ndp* null phenotype implied that Norrin can diffuse from the lens to the retina (Ohlmann et al., 2005). Our demonstration of a strong spatial correlation between XCI territories lacking *Ndp* expression and local loss of the blood-retina barrier implies that endogenous Norrin exhibits minimal diffusion from its site of synthesis in Muller glia. The likely explanation for these apparently contradictory results is that the level of Norrin production by the lens transgene was many orders of magnitude greater than production from the endogenous *Ndp* gene (Ohlmann et al., 2005; Ye et al., 2011), and that very small quantities of Norrin suffice for biological rescue. Our data suggest that the variable clinical phenotypes of *NDP* carrier females could arise from variable XCI skewing and/or variations in XCI topography in the context of limited diffusion of Norrin within the retina.

As noted in the Introduction, mosaic expression of polymorphic cone pigment genes in the retinas of New World primates and genetically engineered mice endows heterozygous females with novel color vision capabilities. Could mosaic expression of other genes also confer a functional advantage? One could argue that the New World primate case is unusual because the polymorphic variants shift receptor spectral sensitivity, whereas most genetic variation has either no effect or impairs protein function. However, the following model suggests that XCI mosaicism in the nervous system could be associated more generally with a functional advantage. Consider a neural ensemble composed of several hundred cells, and a polymorphic X-linked gene that influences the stimulus-response relationship for some or all of the neurons within that ensemble (Figure 8). For example, the gene product might affect the synthesis, release, or recycling of neurotransmitter, the regulation of receptors or second messenger systems, or the resting membrane potential. Depending on which of the polymorphic alleles is present, the

neural ensemble in hemizygous males and homozygous females would exhibit stimulus-response curves that differ in their positions along the stimulus axis (upper two panels of Figure 8). In contrast, in heterozygous females, the same ensemble would be populated by two biochemically distinct types of neurons, as shown in the bottom panel of Figure 8, with the result that the stimulus-response relationship—the ensemble's dynamic range—would likely be expanded along the stimulus axis. Importantly, this outcome is distinct from that predicted for polymorphic variation in an autosomal gene: in the autosomal case, the neural ensemble in heterozygotes would have a stimulus-response curve with the same dynamic range as the two classes of homozygotes, but at an intermediate location along the stimulus axis (third panel of Figure 8).

The model in the preceding paragraph derives its plausibility from the fact that neural computations depend on cellular diversity. A diversity-generating mechanism such as XCI, which operates on all cells within the CNS and creates diversity on a spatial scale that encompasses the scale of local circuits, has the potential to add functionally relevant capabilities. Because XCI affects 50% of the individuals in every species of eutherian mammal and because it epigenetically silences one allele among ~4% of genes, it may represent one of the more significant mechanisms by which individual differences in CNS function are generated.

EXPERIMENTAL PROCEDURES

Hprt Knockin Reporters

Targeting constructs were prepared by inserting *CAG-LSL-nlsGFP* or *CAG-LSL-nlstdT* cassettes with *Asc* I and *Fse* I ends into plasmid *pDC282-rev HprtV2xcHS4* (Ciavatta et al., 2006) in which the polylinker had been modified to accept *Asc* I-*Fse* I fragments. *Hprt* null mouse embryonic stem cells (Yang et al., 2009) were electroporated with the linearized targeting constructs, selected in HAT medium, and screened by Southern blot hybridization.

Mouse Lines and Breeding Strategies

Table S1 lists the *Cre* lines used in this work. Mice were handled in accordance with the Institutional Animal Care and Use Committee (IACUC) guidelines of the Johns Hopkins Medical Institutions.

Tissue Processing and Immunohistochemistry

For adult tissues (harvested at ~P30, or for adult retinal vasculature at >P42), mice were perfused via a transcardial route with 4% paraformaldehyde (PFA)/PBS. E7.5–E17.5 embryos were fixed by overnight immersion in 4% PFA/PBS at 4°C. Fixed tissues were either imaged intact or vibratome sectioned at 50–150 um thickness. For retinal neuron analysis, retinas were dissected and flat mounted from P2–P15 or P30 eyes that were immersion fixed in 4% paraformaldehyde/PBS at room temperature for 1 hr. For retinal vascular analysis, retinas were fixed overnight in 2% PFA/PBS and then immunostained with rabbit anti-GFP antibody. Cochlea were dissected from P5 mouse heads that were immersion fixed in 4% paraformaldehyde/PBS overnight at 4°C. For cryosectioning (12 um thickness), tissues were equilibrated in 30% sucrose/PBS prior to embedding in optimal cutting temperature (OCT) compound. Antibodies are listed in Table S4.

Microscopy and Image Analysis

Images were captured on a Zeiss LSM700 confocal microscope and processed with Zen software, ImageJ/Fiji, and Adobe Photoshop. Automated and manual methods of cell identification are described in the Supplemental Experimental Procedures.

Modeling

Modeling of cone development is described in the Supplemental Experimental Procedures.

RNA-seq

Two crosses were performed: female *M. castaneous* x male *M. musculus* ($Hprt^{tdT}$) and male *M. castaneous* x female *M. musculus* ($Hprt^{tdT/tdT}$). Brains from P0 female progeny were dissected, cells were gently dissociated with papain (Worthington Biochemicals), and tdT+ and tdT− populations were separated by FACS (Figures 7 and S5) and processed for RNA-seq as described in the Supplemental Experimental Procedures.

SUPPLEMENTAL INFORMATION

Supplemental Information includes Supplemental Experimental Procedures, six figures, and five tables and can be found with this article online at http://dx.doi.org/10.1016/j.neuron.2013.10.051.

ACKNOWLEDGMENTS

The authors thank Elizabeth Simpson for the gift of *Hprt* mutant ES cells, Dominic Ciavatta for the *Hprt* targeting vector, Dwight Bergles, Karl Deisseroth, Alex Kolodkin, and Se-Jin Lee for *Cre* lines, Terry Shelley for custom manufacturing support, the members of the Johns Hopkins Transgenic, Flow Cytometry, and NextGen Sequencing core facilities for blastocyst injection, FACS sorting, and RNA-seq library construction, John Williams for assistance with genotyping, and Rudolf Jaenisch, Lucas Hua, Barbara Migeon, and Max Tischfield for helpful discussions and/or comments on the manuscript. Supported by National Institutes of Health P30 CA006973 (S.J.W.), the Human Frontier Science Program (H.W.), the Howard Hughes Medical Institute, and the Brain Sciences Institute of the Johns Hopkins University.

Accepted: October 10, 2013
Published: January 8, 2014

REFERENCES

Abecasis, G.R., Auton, A., Brooks, L.D., DePristo, M.A., Durbin, R.M., Handsaker, R.E., Kang, H.M., Marth, G.T., and McVean, G.A.; 1000 Genomes Project Consortium (2012). An integrated map of genetic variation from 1,092 human genomes. Nature *491*, 56–65.

Amos-Landgraf, J.M., Cottle, A., Plenge, R.M., Friez, M., Schwartz, C.E., Longshore, J., and Willard, H.F. (2006). X chromosome-inactivation patterns of 1,005 phenotypically unaffected females. Am. J. Hum. Genet. *79*, 493–499.

Berger, W., and Ropers, H.H. (2001). Norrie disease. In Metabolic and Molecular Bases of Inherited Disease, Eighth Edition, C.R. Scriver, A.L. Beaudet, W.S. Sly, and D. Valle, eds. (New York: McGraw Hill), pp. 5977–5985.

Carrel, L., and Willard, H.F. (2005). X-inactivation profile reveals extensive variability in X-linked gene expression in females. Nature *434*, 400–404.

Cattanach, B.M. (1975). Control of chromosome inactivation. Annu. Rev. Genet. *9*, 1–18.

Chahrour, M., and Zoghbi, H.Y. (2007). The story of Rett syndrome: from clinic to neurobiology. Neuron *56*, 422–437.

Chonchaiya, W., Nguyen, D.V., Au, J., Campos, L., Berry-Kravis, E.M., Lohse, K., Mu, Y., Utari, A., Hervey, C., Wang, L., et al. (2010). Clinical involvement in daughters of men with fragile X-associated tremor ataxia syndrome. Clin. Genet. *78*, 38–46.

Chung, I.M., Schwartz, S.M., and Murry, C.E. (1998). Clonal architecture of normal and atherosclerotic aorta: implications for atherogenesis and vascular development. Am. J. Pathol. *152*, 913–923.

Ciavatta, D., Kalantry, S., Magnuson, T., and Smithies, O. (2006). A DNA insulator prevents repression of a targeted X-linked transgene but not its random or imprinted X inactivation. Proc. Natl. Acad. Sci. USA *103*, 9958–9963.

Cohn, S.A., Emmerich, D.S., and Carlson, E.A. (1989). Differences in the responses of heterozygous carriers of colorblindness and normal controls to briefly presented stimuli. Vision Res. *29*, 255–262.

Coussa, R.G., and Traboulsi, E.I. (2012). Choroideremia: a review of general findings and pathogenesis. Ophthalmic Genet. *33*, 57–65.

Dobyns, W.B., Filauro, A., Tomson, B.N., Chan, A.S., Ho, A.W., Ting, N.T., Oosterwijk, J.C., and Ober, C. (2004). Inheritance of most X-linked traits is not dominant or recessive, just X-linked. Am. J. Med. Genet. A. *129A*, 136–143.

Fekete, D.M., Perez-Miguelsanz, J., Ryder, E.F., and Cepko, C.L. (1994). Clonal analysis in the chicken retina reveals tangential dispersion of clonally related cells. Dev. Biol. *166*, 666–682.

Fruttiger, M. (2007). Development of the retinal vasculature. Angiogenesis *10*, 77–88.

Fu, W., O'Connor, T.D., Jun, G., Kang, H.M., Abecasis, G., Leal, S.M., Gabriel, S., Rieder, M.J., Altshuler, D., Shendure, J., et al.; NHLBI Exome Sequencing Project (2013). Analysis of 6,515 exomes reveals the recent origin of most human protein-coding variants. Nature *493*, 216–220.

Gregg, C., Zhang, J., Butler, J.E., Haig, D., and Dulac, C. (2010). Sex-specific parent-of-origin allelic expression in the mouse brain. Science *329*, 682–685.

Grover, S., Fishman, G.A., Anderson, R.J., and Lindeman, M. (2000). A longitudinal study of visual function in carriers of X-linked recessive retinitis pigmentosa. Ophthalmology *107*, 386–396.

Hadjantonakis, A.K., Cox, L.L., Tam, P.P., and Nagy, A. (2001). An X-linked GFP transgene reveals unexpected paternal X-chromosome activity in trophoblastic giant cells of the mouse placenta. Genesis *29*, 133–140.

Jacobs, G.H. (1998). A perspective on color vision in platyrrhine monkeys. Vision Res. *38*, 3307–3313.

Jacobs, G.H., Williams, G.A., Cahill, H., and Nathans, J. (2007). Emergence of novel color vision in mice engineered to express a human cone photopigment. Science *315*, 1723–1725.

Jais, J.P., Knebelmann, B., Giatras, I., De Marchi, M., Rizzoni, G., Renieri, A., Weber, M., Gross, O., Netzer, K.O., Flinter, F., et al. (2003). X-linked Alport syndrome: natural history and genotype-phenotype correlations in girls and women belonging to 195 families: a "European Community Alport Syndrome Concerted Action" study. J. Am. Soc. Nephrol. *14*, 2603–2610.

Jakobsson, L., Franco, C.A., Bentley, K., Collins, R.T., Ponsioen, B., Aspalter, I.M., Rosewell, I., Busse, M., Thurston, G., Medvinsky, A., et al. (2010). Endothelial cells dynamically compete for the tip cell position during angiogenic sprouting. Nat. Cell Biol. *12*, 943–953.

Jan, T.A., Lu, L., Li, C.X., Williams, R.W., and Waters, R.S. (2008). Genetic analysis of posterior medial barrel subfield (PMBSF) size in somatosensory cortex (SI) in recombinant inbred strains of mice. BMC Neurosci. *9*, 3.

Jangouk, P., Zackowski, K.M., Naidu, S., and Raymond, G.V. (2012). Adrenoleukodystrophy in female heterozygotes: underrecognized and undertreated. Mol. Genet. Metab. *105*, 180–185.

Jinnah, H.A., and Friedmann, T. (2001). Lesch-Nyhan disease and its variants. In The Metabolic and Molecular Bases of Inherited Disease, Eighth Edition, C.R. Scriver, A.L. Baudet, W.S. Sly, D. Valle, B. Childs, K.W. Kinzler, and B. Vogelstein, eds. (New York: McGraw Hill), pp. 2537–2570.

Lee, J.T. (2011). Gracefully ageing at 50, X-chromosome inactivation becomes a paradigm for RNA and chromatin control. Nat. Rev. Mol. Cell Biol. *12*, 815–826.

Levin, M. (2005). Left-right asymmetry in embryonic development: a comprehensive review. Mech. Dev. *122*, 3–25.

Li, S.M., Valo, Z., Wang, J., Gao, H., Bowers, C.W., and Singer-Sam, J. (2012). Transcriptome-wide survey of mouse CNS-derived cells reveals monoallelic expression within novel gene families. PLoS ONE *7*, e31751.

Lin, P., Shankar, S.P., Duncan, J., Slavotinek, A., Stone, E.M., and Rutar, T. (2010). Retinal vascular abnormalities and dragged maculae in a carrier with a new NDP mutation (c.268delC) that caused severe Norrie disease in the proband. J. AAPOS *14*, 93–96.

Liu, X., Han, D., Li, J., Han, B., Ouyang, X., Cheng, J., Li, X., Jin, Z., Wang, Y., Bitner-Glindzicz, M., et al. (2010). Loss-of-function mutations in the PRPS1 gene cause a type of nonsyndromic X-linked sensorineural deafness, DFN2. Am. J. Hum. Genet. *86*, 65–71.

Liu, X.Z., Xie, D., Yuan, H.J., de Brouwer, A.P., Christodoulou, J., and Yan, D. (2013). Hearing loss and PRPS1 mutations: wide spectrum of phenotypes and potential therapy. Int. J. Audiol. *52*, 23–28.

Lyon, M.F. (1962). Sex chromatin and gene action in the mammalian X-chromosome. Am. J. Hum. Genet. *14*, 135–148.

Molnár, Z., and Clowry, G. (2012). Cerebral cortical development in rodents and primates. Prog. Brain Res. *195*, 45–70.

Ohlmann, A., Scholz, M., Goldwich, A., Chauhan, B.K., Hudl, K., Ohlmann, A.V., Zrenner, E., Berger, W., Cvekl, A., Seeliger, M.W., and Tamm, E.R. (2005). Ectopic Norrin induces growth of ocular capillaries and restores normal retinal angiogenesis in Norrie disease mutant mice. J. Neurosci. *25*, 1701–1710.

Parnavelas, J.G. (2000). The origin and migration of cortical neurones: new vistas. Trends Neurosci. *23*, 126–131.

Pinter, S.F., Sadreyev, R.I., Yildirim, E., Jeon, Y., Ohsumi, T.K., Borowsky, M., and Lee, J.T. (2012). Spreading of X chromosome inactivation via a hierarchy of defined Polycomb stations. Genome Res. *22*, 1864–1876.

Ramírez, A., Milot, E., Ponsa, I., Marcos-Gutiérrez, C., Page, A., Santos, M., Jorcano, J., and Vidal, M. (2001). Sequence and chromosomal context effects on variegated expression of keratin 5/lacZ constructs in stratified epithelia of transgenic mice. Genetics *158*, 341–350.

Reese, B.E., Necessary, B.D., Tam, P.P., Faulkner-Jones, B., and Tan, S.S. (1999). Clonal expansion and cell dispersion in the developing mouse retina. Eur. J. Neurosci. *11*, 2965–2978.

Rodieck, R.W. (1991). The density recovery profile: a method for the analysis of points in the plane applicable to retinal studies. Vis. Neurosci. *6*, 95–111.

Sims, K.B., Irvine, A.R., and Good, W.V. (1997). Norrie disease in a family with a manifesting female carrier. Arch. Ophthalmol. *115*, 517–519.

Sperry, R. (1982). Some effects of disconnecting the cerebral hemispheres. Science *217*, 1223–1226.

Stenman, J.M., Rajagopal, J., Carroll, T.J., Ishibashi, M., McMahon, J., and McMahon, A.P. (2008). Canonical Wnt signaling regulates organ-specific assembly and differentiation of CNS vasculature. Science *322*, 1247–1250.

Sugimoto, M., Tan, S.S., and Takagi, N. (2000). X chromosome inactivation revealed by the X-linked lacZ transgene activity in periimplantation mouse embryos. Int. J. Dev. Biol. *44*, 177–182.

Takagi, N., and Sasaki, M. (1975). Preferential inactivation of the paternally derived X chromosome in the extraembryonic membranes of the mouse. Nature *256*, 640–642.

Tan, S.S., Williams, E.A., and Tam, P.P. (1993). X-chromosome inactivation occurs at different times in different tissues of the post-implantation mouse embryo. Nat. Genet. *3*, 170–174.

Tan, S.S., Kalloniatis, M., Sturm, K., Tam, P.P., Reese, B.E., and Faulkner-Jones, B. (1998). Separate progenitors for radial and tangential cell dispersion during development of the cerebral neocortex. Neuron *21*, 295–304.

Tassone, F., Greco, C.M., Hunsaker, M.R., Seritan, A.L., Berman, R.F., Gane, L.W., Jacquemont, S., Basuta, K., Jin, L.W., Hagerman, P.J., and Hagerman, R.J. (2012). Neuropathological, clinical and molecular pathology in female fragile X premutation carriers with and without FXTAS. Genes Brain Behav. *11*, 577–585.

Thorvaldsen, J.L., Krapp, C., Willard, H.F., and Bartolomei, M.S. (2012). Nonrandom X chromosome inactivation is influenced by multiple regions on the murine X chromosome. Genetics *192*, 1095–1107.

Wang, Y., Rattner, A., Zhou, Y., Williams, J., Smallwood, P.M., and Nathans, J. (2012). Norrin/Frizzled4 signaling in retinal vascular development and blood brain barrier plasticity. Cell *151*, 1332–1344.

West, J.D., Frels, W.I., Chapman, V.M., and Papaioannou, V.E. (1977). Preferential expression of the maternally derived X chromosome in the mouse yolk sac. Cell *12*, 873–882.

Willard, H.F. (2001). The sex chromosomes and X chromosome inactivation. In The Metabolic and Molecular Bases of Inherited Disease, Eighth Edition, C.R. Scriver, A.L. Baudet, W.S. Sly, D. Valle, B. Childs, K.W. Kinzler, and B. Vogelstein, eds. (New York: McGraw Hill), pp. 1191–1211.

Wonders, C.P., and Anderson, S.A. (2006). The origin and specification of cortical interneurons. Nat. Rev. Neurosci. *7*, 687–696.

Yang, G.S., Banks, K.G., Bonaguro, R.J., Wilson, G., Dreolini, L., de Leeuw, C.N., Liu, L., Swanson, D.J., Goldowitz, D., Holt, R.A., and Simpson, E.M. (2009). Next generation tools for high-throughput promoter and expression analysis employing single-copy knock-ins at the *Hprt1* locus. Genomics *93*, 196–204.

Yang, F., Babak, T., Shendure, J., and Disteche, C.M. (2010). Global survey of escape from X inactivation by RNA-sequencing in mouse. Genome Res. *20*, 614–622.

Ye, X., Wang, Y., and Nathans, J. (2010). The Norrin/Frizzled4 signaling pathway in retinal vascular development and disease. Trends Mol. Med. *16*, 417–425.

Ye, X., Smallwood, P., and Nathans, J. (2011). Expression of the Norrie disease gene (Ndp) in developing and adult mouse eye, ear, and brain. Gene Expr. Patterns *11*, 151–155.